Eur. Phys. J. B **28**, 163–171 (2002)
DOI: 10.1140/epjb/e2002-00218-6

THE EUROPEAN PHYSICAL JOURNAL B

Phase transition and random-field induced domain wall response of $SrTi^{18}O_3$

L. Zhang[1], W. Kleemann[1,a], J. Dec[1,b], R. Wang[2], and M. Itoh[2]

[1] Laboratorium für Angewandte Physik, Gerhard Mercator Universität Duisburg, 47048 Duisburg, Germany
[2] Materials and Structures Laboratory, Tokyo Institute of Technology, 4259 Nagatsuta, Midori, Yokohama 226-8503, Japan

Received 4 January 2002 / Received in final form 25 March 2002
Published online 19 July 2002 –

Abstract. The dielectric permittivity $\epsilon' - i\epsilon''$ of $SrTi^{18}O_3$ (STO18) is studied under a dc electric field E as a function of the temperature, T. In ϵ' *vs.* T, a double-peak is found when $0 < E < 30$ KV/m. While the peak at high-T is attributed to the smeared ferroelectric phase transition, the low-T one is induced by domain wall motion. The transverse Ising model including an external homogeneous and quenched random-fields is successfully used to describe both the smeared phase transition and the domain wall response in the low-T domain state. The calculations are in good agreement with the experimental results.

PACS. 77.22.Ch Permittivity (dielectric function) – 77.80.Bh Phase transitions and Curie point – 77.80.Dj Domain structure; hysteresis – 77.84.Dy Niobates, titanates, tantalates, PZT ceramics, etc.

1 Introduction

In the last decade remarkable new results have emerged from studies of $SrTiO_3$ and continue to attract great attention to this most extensively studied perovskite type crystal. $SrTiO_3$ is a typical example of quantum paraelectricity [1–3]. Its static dielectric constant saturates at low temperature at a high level, $\epsilon' \approx 2{\times}10^4$ [1], associated with the softening of a long-wavelength transverse optic phonon mode. Application of uniaxial stress and proper substitution of A site ions can destabilize the lattice significantly and induce a ferroelectric phase transition [4–6]. Additionally, a crossover from quantum ferroelectric to relaxor behavior may occur as observed, *e.g.*, in $(Sr_{1-1.5x}Bi_x)TiO_3$ for $x > 0.027$ [7]. Here the relaxor behavior is attributed to a ferroelectric domain state induced by random fields (RFs) [8].

Recently, Itoh *et al.* [9,10] have demonstrated that ferroelectricity can also be induced by oxygen isotope exchange. A dielectric peak near $T_{m1} \approx 24$ K was detected in a 93% ^{18}O-isotope-exchanged $SrTiO_3$ (STO18) sample. Below T_{m1}, a hysteresis loop indicates that the dielectric peak corresponds to the evolution of ferroelectricity in STO18.

Differently from other ferroelectrics, the Curie point of STO18 appears in the very low-T region. For this reason, quantum mechanical fluctuations are expected to decrease the polarization from a fundamental point of view. In addition, the appearing spontaneous or remanent polarization may be suppressed due to the formation of a RF induced domain state as reported recently [11]. It was shown that external fields increase the permittivity below the Curie point. In ferroelectrics, such behavior is usually attributed to the dynamics of domain walls. Since the relaxation of the field-induced remanent polarization is best fitted by a generalized power law [12], it has been argued that the ferroelectric domain state might be induced by quenched RFs [11].

In this paper, we report on experimental results of the dielectric behavior of STO18 under the action of dc electric fields up to $E = 110$ kV/m. A noticeable additional ϵ' peak with frequency dispersion appears below T_{m1} as $E \neq 0$. The peak temperature, T_{m2}, first decreases, then increases again, until the peak finally disappears at large dc bias. This implies that the low-temperature peak originates from domain wall motion induced by the field.

In order to describe the phase transition of STO18, anharmonic electron-phonon interaction [13] and single-sublattice models [14] have been used to explain the isotope effect in $SrTiO_3$ in terms of a displacive soft-mode mechanism. However, a recent Raman scattering study [15] shows that the ferroelectric soft mode reveals only uncomplete softening of the E_u component of the F_{1u}-type polar optic mode at the Curie point. Similarly as in the related impurity system $Sr_{1-x}Ca_xTiO_3$ (SCT, $x = 0.007$) [16] the softening stops at an energy of about 5 cm^{-1}. This result rather suggests that the ferroelectric phase transition is not a purely displacive one, but becomes order-disorder controlled in the vicinity of T_c. Following previous treatments of the phase transitions

[a] e-mail: wolfgang@kleeman.uni-duisburg.de
[b] *Permanent address:* Institute of Physics. University of Silesia, PL 40-007 Katowice, Poland

in the SCT system [17,18] we therefore suggest to adopt an appropriate order-disorder model for a simplified, albeit not unrealistic description of the phase transition in STO18. We employ the transverse Ising model [19], which has recently been used to explain the phase transitional properties of quantum paraelectrics and quantum ferroelectrics from a macroscopic point of view [17,18,20]. *RF*s are additionally introduced in order to describe the observed domains state properties [21]. Our calculations clearly evidence that local frozen fields give rise to the existence of a ferroelectric multi-domain state, and that the dielectric behavior of STO18 under a bias field has an intimate relationship with the domain wall motion.

2 Experimental procedure

The experiments were performed on a single-crystal sample of $SrTi(^{16}O_{0.08}\ ^{18}O_{0.92})_3$ prepared in the same way as described previously [9], with dimensions $0.3\times3\times7$ mm^3 parallel to the cubic directions [110], [$\bar{1}$10] and [001], respectively, cut from a single crystal. This geometry warrants the formation of a crystallographic single domain with the tetragonal c axis along the long sample edges when cooling to below the antiferrodistortive transition temperature, $T_0 \approx 105$ K [1]. Cationic impurities in the crystal are in the low ppm range as reported previously [22]. The large faces of the sample were covered with copper prior to sputtering deposition of gold. The complex dielectric constant $\epsilon = \epsilon' - \mathrm{i}\epsilon''$ was measured by using a Solartron 1296 dielectric interface and a HP 4192A impedance analyzer, respectively, at frequencies 0.1 Hz $\leq f \leq$ 100 kHz and temperatures 4.5 K $\leq T \leq$ 300 K with *ac* probing fields of 300 V/m in a helium gas-flow cryostat.

Bias fields up to 110 kV/m were applied for measuring the field dependence of the dielectric constant. In the experiment, the sample was first cooled in zero field from 130 to 80 K. During the subsequent measurements, the cooling or heating rates were in the order of 1 K/min, while different bias fields were maintained throughout.

3 Experimental results

Figure 1 shows the temperature dependences of ϵ' and ϵ'' upon field-cooling at selected constant bias fields. The real part of the zero-field dielectric constant ϵ' exhibits a significant peak I at $T_{m1} \approx 24.2$ K corresponding to the ferroelectric phase transition [9,10]. It should be stressed that this peak definitely arises as a consequence of the isotope exchange $^{16}O \rightarrow ^{18}O$ and is not due to some defect structure induced by the preparation procedure. This was verified by recent experiments on samples of STO16, which had experienced the same long-time high-temperature treatment as the STO18 samples albeit in an ordinary $^{16}O_2$ atmosphere [23]. Apart from a slight decrease of the amplitude no change of the original quantum paraelectric susceptibility curve χ' *vs.* T could be observed. In

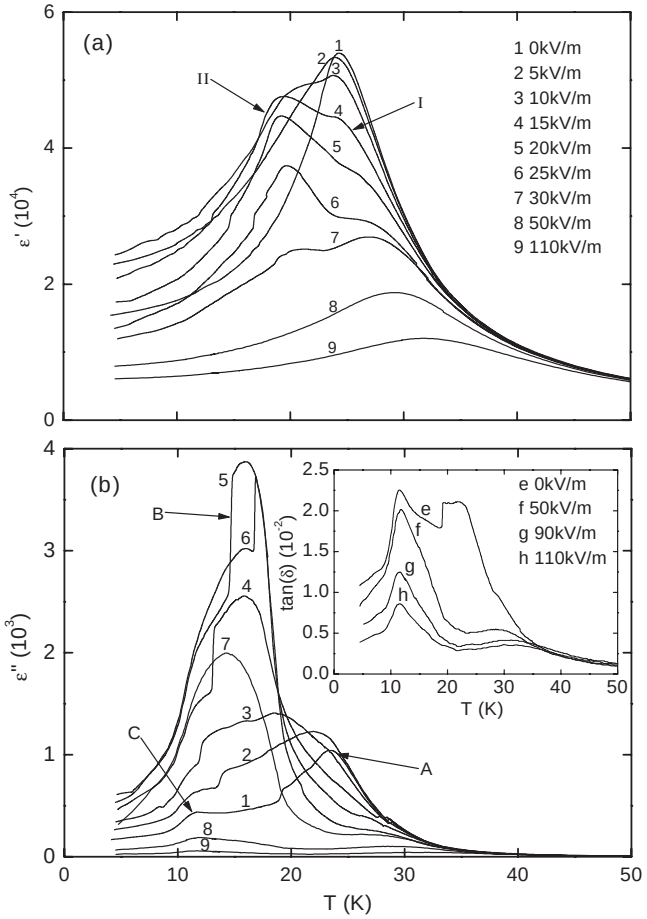

Fig. 1. (a) ϵ' and (b) ϵ'' measured at $f = 10$ kHz in STO18 as a function of temperature at several selected bias fields. Field notations are the same for both (a) and (b). The inset in (b) shows the temperature dependence of $\tan\delta$ at selected bias fields. The arrows point to the positions of the peaks of ϵ', I and II (a), and of ϵ'', A, B and C (b) (see text). The inset to (b) shows $\tan\delta$ *versus* T for selected field values.

Figure 1a, the peak value of ϵ' gradually decreases with increasing bias field from 54 000 ($E = 0$; curve 1) to 11 000 ($E = 110$ kV/m; curve 9), while T_{m1} gradually shifts to higher temperatures (Fig. 2). Upon increasing E, the peak splits into a double-peak, *e.g.* at $T_{m2} \approx 19$ K and $T_{m1} \approx 24$ K for $E = 15$ kV/m. As will be argued below, the peak II at T_{m2} is primarily due to domain wall motion. Hence, upon lowering the temperature to below T_{m2} the dielectric constant rapidly drops as a consequence of domain wall freezing. At higher fields, $E > 15$ kV/m, peak II is gradually suppressed, while T_{m2} remains virtually constant (Fig. 2).

In Figure 1b, curve 1 at $E = 0$ shows two peaks of ϵ'', A and C. Peak A at 23.6 K corresponds to peak I of ϵ' in Figure 1a. It is characteristic of the ferroelectric transition. The weak ϵ'' peak C at $T = 11$ K is by orders of magnitude smaller than the corresponding ϵ' values. Therefore, no changes of ϵ' which might be related to the ϵ'' peak are detectable near 11 K. Conspicuously, similar ϵ'' peaks near 11 K have been found in both $SrTi^{16}O_3$ single crystals [24]

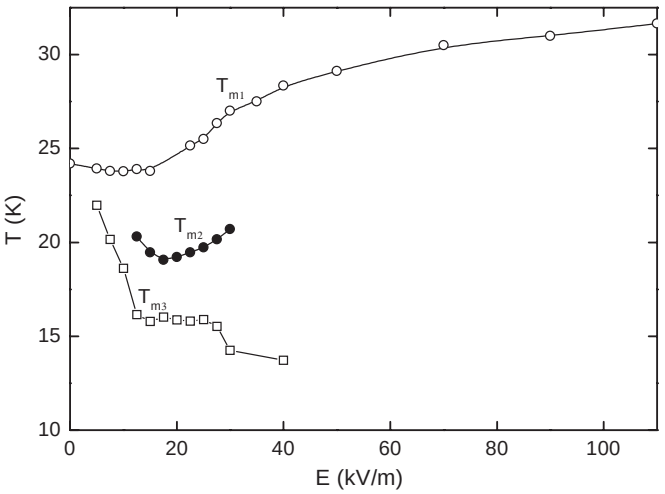

Fig. 2. Field dependencies of T_{m1}, T_{m2} and T_{m3} as defined in the text. The data points are connected by solid lines as guides to the eye.

and films [25]. It seems, hence, plausible to attribute this peak to relaxing impurity dipoles of unknown origin and to ignore its presence in the following.

For $E > 0$ a significant ϵ'' peak B corresponding to the ϵ' peak II is induced. Its position, T_{m3}, is slightly lower than that of T_{m2} (Fig. 2). Upon increasing E, the peak B moves to lower temperature ($T_{m3} \approx 15$ K at $E = 20$ kV/m, curve 5), while the peak values of ϵ'' increases to 3800. At higher fields the peak B becomes gradually suppressed.

Within the range 5 kV/m $< E <$ 30 kV/m, the B peak values of ϵ'' are very large, while peak A is strongly decreasing and peak C is completely covered. Only at $E \geq 50$ kV/m, where the crystal reaches the single-domain state, the peak B is also completely suppressed. The inset of Figure 1b shows the loss factors $\epsilon''/\epsilon' = \tan\delta$ referring to the peaks A and C. The latter one survives electric fields $E \geq 50$ kV/m at constant intensity. While its position is virtually independent of E, only its underground intensity seems to be continuously decreasing. Contrastingly, the A peak position of tanδ shifts to higher T with increasing E, and its peak value gradually decreases. This is characteristic of the ferroelectric peak.

Figure 2 shows the field dependences of T_{m1}, T_{m2} and T_{m3} (as defined above). While T_{m1} increases with increasing bias field as usual for ferroelectrics, T_{m2} first decreases to 19 K and then increases to 21 K. T_{m3} behaves similarly.

For STO18 a non-exponential relaxation of the field-induced remanent polarization [11] has been reported. Correspondingly, polydispersive frequency response of the dielectric constant in STO18 is expected. Figure 3 shows the temperature dependencies of the dielectric permittivity for $f = 1$ Hz and 10 kHz. Obviously, dielectric dispersion is seen to appear only below $T \approx 30$ K, where the real part ϵ' increases with decreasing frequency (Fig. 3a). The imaginary part ϵ'' shows a peak at lower temperatures and higher values at lower frequencies.

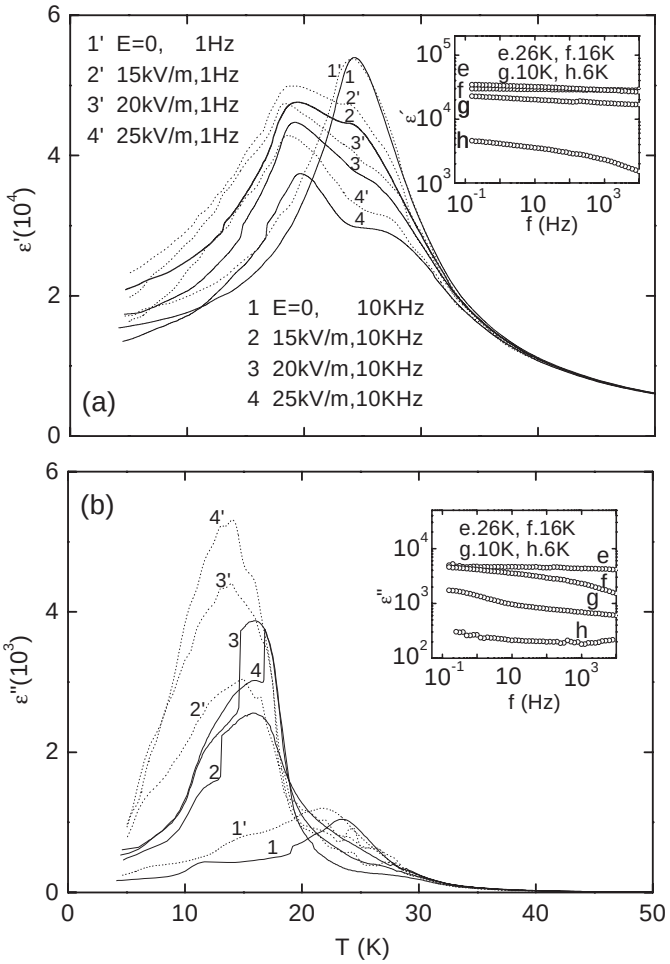

Fig. 3. Temperature dependence of (a) ϵ' and (b) ϵ'' at selected bias fields. Solid lines (curve 1–4) are for $f = 10$ kHz; dashed lines (curve 1′–4′) are for $f = 1$ Hz. The insets show the frequency dispersion of $\epsilon'$and ϵ'' for various T values.

The insets to Figures 3a and b show spectra of ϵ' and ϵ'' *vs.* f, respectively, in double-logarithmic plots. They have been taken in an external field $E = 25$ kV/m at various fixed temperatures, $T = 6$, 10, 16 and 26 K, and frequencies $0.1 \leq f \leq 10^4$ Hz. It is seen that both ϵ' and ϵ'' decrease monotonically with increasing f, a signature which has also been observed on relaxor ferroelectrics [27]. In our case we attribute such behavior to irreversible domain wall displacements as will be discussed in detail elsewhere [28]. In the present paper we shall restrict ourselves to explain the static dielectric response of the nanodomain state.

4 Model and discussion

4.1 Hamiltonian

The motion of the Ti^{4+} ions in their ^{18}O octahedral environment is treated within the framework of the quantum mechanical transverse Ising model [19], which readily yields Barrett's successful formula [29] of ϵ' *vs.* T for

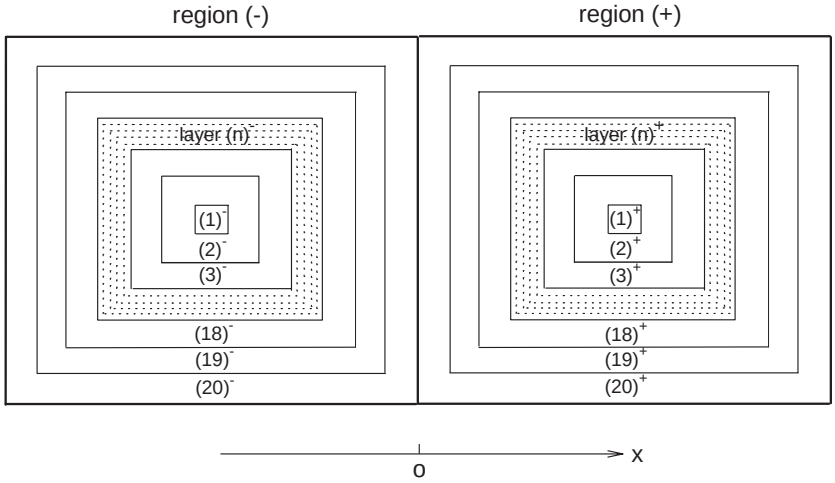

Fig. 4. Central cross section of two adjacent nano-domains (individual volume = $(39a)^3$, a = lattice constant) with their shell structure at $E = 0$ as defined in the text.

STO16, say, [30] and appears as an acceptable first approximation to model the order-disorder aspect of the ferroelectric phase transition of STO18 in view of the absence of complete mode softening [15]. In addition to an external applied field E, we consider the existence of quenched random-fields, $E_{\rm i}$, which might be due to frozen dipolar impurities or ionic vacancies as conjectured previously in the case of Ca-doped STO16 [31]. In the case of heavily heat-treated STO18 in a $^{18}O_2$ atmosphere [9] an excess of strontium vacancies seems particularly probable [32]. They are equivalent to an excess of negative ions, which give rise to quenched electric fields in addition to those of the dipolar impurities.

In order to treat the interactions of the dipolar moments as well as the quantum mechanical effects in a unified framework we use the Hamiltonian

$$\mathbf{H} = -\Omega \sum_i S_i^x - \frac{1}{2} \sum_{ij} J_{ij} S_i^z S_j^z - 2\mu \sum_i (E + E_i) S_i^z \tag{1}$$

where $S_i^x (S_i^z)$ are the $x(z)$ components of the pseudo-spins and i and j sum over all pseudo-spins, which are proposed to correspond to the displacement of titanium with respect to the oxygen octahedron. Ω, $J = \sum j J_{ij}$ and μ are the tunneling frequency, the interaction constant and the effective dipolar moment, respectively. While E stands for the homogeneous external field, E_i is the site-dependent RF.

4.2 Basic model

In a real system, the numerical solution of equation (1) is very difficult. It comprises transverse, normal and random fields simultaneously. Thus we are urged to introduce some simplifying suppositions.

First, we replace the original perovskite lattice by a simple cubic NaCl-type lattice, where the coordination number of an elementary cell is 6. We thus disregard the tetragonal distortion at low T and the effective xy symmetry of the polar order parameter [5].

Second, we introduce a coarse-graining of the RF distribution. We merely consider their fluctuations, which are due to the statistical impurity distribution. Hence, in small enough regions, the average RF will deviate from zero, $\langle E_{\rm i} \rangle = E_{\rm frozen}$. These fluctuations, henceforth denoted as "*frozen field*", $E_{\rm frozen}$, are fundamental for the physical picture of nanodomains. It assumes that frozen fields of either sign exist in different nanoscopic regions [26]. When the frozen field changes its direction, the direction of the polarization of the microscopic region will also change. In this reasoning the cost of energy by domain walls is considered to be compensated by large enough domain volumes [26]. At the first glance this definition looks quite arbitrary, since any temperature dependence of the RF-induced domains [33] is excluded. However, as is well-known from experimental studies on real RF systems, as *e.g.* diluted antiferromagnets cooled to below T_N in an external magnetic field [34], extreme slowing-down of the dynamics gives rise to metastable nanodomain structures when approaching T_N. Thus virtually invariable domain structures are encountered upon further cooling.

In our model, we subdivide the crystal into a superlattice of cubic regions with the same size. Figure 4 shows a cross-section through two adjacent regions in $E = 0$. We define as region $(+)$ the region with a positive frozen field, and as region $(-)$ the region with negative frozen field. The linear width of these regions is set to the arbitrary, but realistic nanosize $39a$ along all Cartesian coordinates, x, y and z, where a is the lattice constant. As will be mentioned in Section 4, the average size of the domains crucially determines the weight of the domain wall response at $T < T_{m1}$. It is left for future investigations to determine the optimal domain size according to this best-fit criterion.

Below we shall calculate the local molecular fields in a selfconsistent way similarly as done recently in the case of quantum paraelectrics doped with point-defects [17].

In the present case planar defects (discontinuity planes of $E_{\rm frozen}$) have to be dealt with. For this reason it appears reasonable to consider groups of equivalent spins experiencing the same molecular field in the following way. In Figure 4, the regions (+) and (−) are each divided into 20 concentric shells with width a. From the cubic center to the boundary, region (+) comprises the shells $(n)^+$, while region (−) consists of the shells (n^-), $1 \leq n \leq 20$. By this procedure it is taken into account that the polarization is smallest near the edges of the regions, while it becomes larger near their centers.

Now we discuss the average pseudo-spin interaction constants in different shells of region (+). In the central "shell" $(1)^+$, the number of pseudo-spins is 1. Its total number of bonds with adjacent pseudo-spins is 6 (4 in-plane and 2 out-of plane). Thus the molecular field $\overline{E}_{\rm a}\,|_{{\rm shell}(1)^+}$ in the shell $(1)^+$ is

$$\overline{E}_{a1} = \overline{\sum_i JS_i^z} = J\langle S_i^z\rangle_{(2)^+} \tag{2}$$

where $\langle S_i^z\rangle\,|_{(2)^+}$ is the average value of the spins in shell $(2)^+$.

In shell $(n)^+$, $2 \leq n \leq 19$, the number of pseudo-spins is $24n^2-48n+26$, and the total bond numbers with shells $(n-1)^+$, $(n)^+$ and $(n+1)^+$ are $24n^2-72n+54$, $96n^2-192n+96$ and $24n^2-24n+6$ respectively. Thus the molecular field $\overline{E}_a$ in shell $(n)^+$ is

$$\begin{aligned}\overline{E}_{an} &= \overline{\sum_{(n-1)^+} JS_i^z + \sum_{(n)^+} JS_i^z + \sum_{(n+1)^+} JS_i^z} \\ &= \frac{(4n^2-12n+9)J\langle S_i^z\rangle_{(n-1)^+}}{(24n^2-48n+26)} \\ &\quad + \frac{(16n^2-32n+16)J\langle S_i^z\rangle_{(n)^+}}{(24n^2-48n+26)} \\ &\quad + \frac{(4n^2-4n+1)J\langle S_i^z\rangle_{(n+1)^+}}{(24n^2-48n+26)}\end{aligned} \tag{3}$$

where $\langle S_i^z\rangle_{(n-1)^+}$, $\langle S_i^z\rangle_{(n^+)}$ and $\langle S_i^z\rangle_{(n+1)^+}$ are the average value of the spins in the shells $(n-1)^+$, $(n)^+$ and $(n+1)^+$ respectively.

In shell $(20)^+$, the number of pseudo-spins is 8666. The total bond numbers with shells $(19)^+$ and $(20)^+$ are 8214 and 34656 respectively. In addition, in shell $(20)^+$ the spins have interactions with 9126 spins of six neighboring regions. We suppose that $\overline{\langle S_i^z\rangle}_{(20)^+}$ is the average spin of the six shells $(20)^\pm$ in the six neighboring region $(\pm)$. Thus the molecular field $\overline{E}_{a2}$ in the shell $(20)^+$ is

$$\begin{aligned}\overline{E}_{a20} &= \overline{\sum_{(19)^+} JS_i^z + \sum_{(20)^+} JS_i^z + \sum_{(20)^\pm} JS_i^z} \\ &= \frac{1369J\langle S_i^z\rangle_{(19)^+} + 5776J\langle S_i^z\rangle_{(20)^+}}{8666} \\ &\quad + \frac{1521J\overline{\langle S_i^z\rangle}_{(20)^\pm}}{8666}.\end{aligned} \tag{4}$$

The probability that one nano-domain has a positive (negative) frozen field is 50%. Thus we can suppose an average spin $\overline{\langle S_i^z\rangle} = 0.5\langle S_i^z\rangle_{(20)^+} + 0.5\langle S_i^z\rangle_{(20)^-}$, where $\langle S_i^z\rangle_{(20)^-}$ is the spin in shell $(20)^-$. For $E=0$, we expect $\langle S_i^z\rangle_{(20)^+} = -\langle S_i^z\rangle_{(20)^+}$, hence $\overline{\langle S_i^z\rangle} = 0$, thus canceling the last term in equation (4). Hence, within statistical average "closed" boundary conditions are encountered. It should be noticed, however, that $\overline{\langle S_i^z\rangle}$ will deviate from zero for $E>0$. The interaction among nano-domains will then become very important.

According to the average-field approximation, $\langle S_i^z\rangle$ in shell $(1)^+$ is

$$\langle S_{\rm i}^{\rm z}\rangle_{(1)^+} = \frac{\overline{E}_{\rm a1}+2\mu E+2\mu E_{\rm frozen}}{h_1}\tanh\left(\frac{h_1}{2kT}\right) \tag{5}$$

where $h_1 = \sqrt{\Omega^2 + \left[\overline{E}_{\rm a1}+2\mu E+2\mu E_{\rm frozen}\right]^2}$. $\langle S_i^z\rangle$ in shell $(n)^+$ is

$$\langle S_i^z\rangle_{({\rm n})^+} = \frac{\overline{E}_{\rm an}+2\mu E+2\mu E_{\rm frozen}}{h_{\rm n}}\tanh\left(\frac{h_{\rm n}}{2kT}\right) \tag{6}$$

where $h_{\rm n} = \sqrt{\Omega^2 + \left[\overline{E}_{\rm an}+2\mu E+2\mu E_{\rm frozen}\right]^2}$. $\langle S_i^z\rangle$ in shell $(20)^+$ is

$$\langle S_{\rm i}^{\rm z}\rangle_{(20)^+} = \frac{\overline{E}_{\rm a20}+2\mu E+2\mu E_{\rm frozen}}{h_{20}}\tanh\left(\frac{h_{20}}{2kT}\right) \tag{7}$$

where $h_{20} = \sqrt{\Omega^2 + \left[\overline{E}_{\rm a20}+2\mu E+2\mu E_{\rm frozen}\right]^2}$.

Similarly to the above deduction we obtain the values of $\langle S_i^z\rangle_{(1)^-}$, $\langle S_i^z\rangle_{(n)^-}$ and $\langle S_i^z\rangle_{(20)^-}$ in region (−), where $E_{\rm frozen}$ is replaced by $-E_{\rm frozen}$.

For $SrTi^{16}O_3$ it was suggested [20] that the atomic positions in adjacent cells are correlated. As a consequence, a finite dipolar correlation renormalizes the dielectric behavior of $SrTi^{16}O_3$. In this paper we adopt the same supposition. The relaxation proceeds *via* clusters of dipolar moments rather than *via* single dipolar jumps. Thus the dipolar moment obtained from a fit of the theory to the experimental data will be $\mu = \xi\mu_0$, where ξ is the number of dipolar moments in a cluster and μ_0 the actual dipolar moment in the crystal.

The average polarization P in the crystal is

$$\begin{aligned}P &= 2\sum_{\rm i=0}^{\infty}\langle S_i^z\rangle N\mu_0 \\ &= 2\left(\sum_{(+)}\langle S_i^z\rangle + \sum_{(-)}\langle S_i^z\rangle\right)N\mu_0 N_1\end{aligned} \tag{8}$$

where N is the density of dipolar moments, N_1 the total number of spins in one region (+) or (−), where self-consistent solutions for $\langle S_i^z\rangle$ are obtained numerically. The dielectric susceptibility of the crystal can then be obtained by differentiating equation (8) with respect to a negligibly weak uniform electric field.

4.3 Dielectric response

According to equations (2–8) we have obtained the temperature dependence of the dielectric constant of STO18 by properly adjusting ξ, μ_0, Ω, J and $E_{\rm frozen}$. Best-fit procedures to the curves measured at $E = 0$ and 110 kV/m by systematically varying all parameters starting with those of STO-16 [20] yield $\xi = 7.5$, $\mu_0 = 1.84$ e Å, $J/k_B = 152.8$ K, $\Omega/k_B = 68.0$ K and $E_{\rm frozen} = \pm 20$ kV/m. As shown in Figure 5 the theoretical results are in good agreement with the experimental ones. Here we notice that J and Ω primarily determine the peak positions, while $\xi\mu_0$ and $E_{\rm frozen}$ are responsible for the heights and the widths of the curves, respectively.

The theoretical zero-field dielectric constant ϵ' exhibits a peak at $T \approx 24$ K. Surprisingly, with increasing E a second peak emerges and moves to $T_{m2} \approx 19$ K strongly enhanced with respect to the peak at T_{m1}, which takes the role of a shoulder. All of these features are in full agreement with the experimental observations, while only the amplitudes in weak fields (curves 4 and 5) appear exaggerated in the simulations. At higher fields the dielectric peak shifts again to higher temperature ($T_{m1} \approx 32$ K at $E = 110$ kV/m, curve 9) and is gradually suppressed. At $T = 0$, the zero-field dielectric constant ϵ' is about 17 000. With increasing field, the ground-state ϵ' gradually increases to 22 000 ($E = 13.7$ kV/m, curve 4). At higher fields, the ground-state ϵ' begins to decrease step by step. These characteristics closely agree with the experimental curves of Figure 1a.

The above best-fitted parameters have to be compared with those obtained for pure $SrTi^{16}O_3$, $J/k_B = 152$ K and $\Omega/k_B = 84$ K [20,35]. Obviously the oxygen isotope in STO18 does not change the interaction constant, but decreases the tunneling frequency appreciably. The former means that the substitution of ^{18}O will not change the interaction between the oxygen and titanium. This can easily be accepted, as $^{18}O^{2-}$ and $^{16}O^{2-}$ ions have the same electric charge and polarizability. This is different for the tunneling frequency of the Ti^{4+} ion, which substantially decreases when replacing its ^{16}O neighbors by more massive ^{18}O ones. Obviously both the height and the width of the tunneling barrier become enhanced. Indeed, when considering simple Gamow-type tunneling rates, $\Omega \propto \exp(-\alpha m^{1/2})$, $\alpha =$ const., $m =$ atomic mass of oxygen, in a coordinate frame, where the oxygen ions are tunneling with respect to the fixed central Ti^{4+} ion, $\ln(1/\Omega)$ is expected to vary as $m^{1/2}$ when changing the oxygen isotopes. This is corroborated by our results, where $\ln(1/\Omega)$ and $m^{1/2}$ change by 5% and 6%, respectively, upon exchange of $^{16}O \rightarrow {}^{18}O$.

According to our model, the average frozen field $E_{\rm frozen}$ induces the existence of nano-domains in STO18. An interesting extension of the model is to describe the phase transition of an ideal STO18 crystal ($E_{\rm frozen} = 0$) . The inset of Figure 5 shows the comparison between the ferroelectric peaks of the factual STO18 crystal (a: $|E_{\rm frozen}| =$ 20 kV/m) and the ideal STO18 crystal in the absence of *RF*s (b: $E_{\rm frozen} = 0$). The Curie point of the divergence b, $T_{m1} = 23.7$ K, lies slightly below that of peak a, $T_{m1} = 24.2$ K. At high temperatures, both curves coincide. However, because of the existence of $E_{\rm frozen}$, the permittivity of the crystal is considerably lower than that of the ideal crystal in the vicinity of T_c. At low temperatures, $T < 20$ K, however, the tendency is opposite. Due to the frozen fields nanodomains are stabilized, which increase ϵ'.

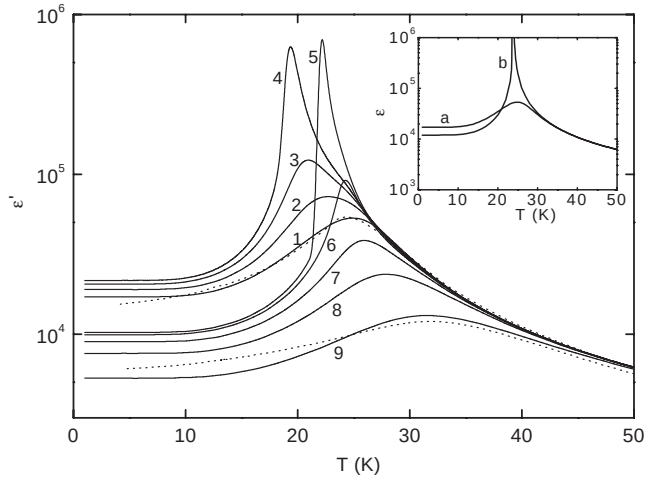

Fig. 5. ϵ' *versus* T curves of STO18 under different bias fields, $E = 0$ (1), 10 (2), 12.5 (3), 13.7 (4), 17 (5), 20 (6), 30 (7), 50 (8) and 110 kV/m (9). The solid and dashed lines are theoretical and experimental results, respectively. The inset show results for $E = 0$ and $|E_{\rm frozen}| = 0$ (b) and 20 kV/m (a).

It is interesting to investigate local properties of our nanodomain model in order to understand the role of the frozen field within the domains and at their walls, respectively. Owing to the selfconsistency of our computational method we are able to determine not only the local order parameter $\langle S_i^z \rangle$, but also its local dielectric response [21]. This is depicted in Figure 6a as a function of temperature for zero external field, $E = 0$, on the central line (x, 0, 0) of the elementary double-cube of Figure 4, where $-20a \leq x \leq +20a$. Two features distinguish the properties of the wall region, $x \approx 0$, from those of the bulk, $|\ x\ | > 0$: (i) the wall permittivity is considerably enhanced as shown for $T = T_m$ and $T = 0$ in Figure 6b, and (ii) its peak appears at significantly lower temperatures, $T_m(x = 0) = 22.7$ K $< T_m(x = \pm 19.5a) = 26.5$ K (Fig. 6b). Both properties are readily explained by the different degrees of polar order within a nanodomain (high T_m, low ϵ') and in its wall regime (low T_m, high ϵ').

4.4 Domain wall motion

Experimentally it is found (Fig. 1) that the dielectric constant increases with increasing bias field for $0 \leq E \leq 15$ kV/m. When $E \geq 20$ kV/m, the dielectric constant decreases with increasing bias field. This phenomenon is explained in a most plausible way by our model, which introduces local random fields in the order $E_{\rm frozen} \approx 20$ kV/m. These are believed to pin the domain walls until they are overcome by the external field in

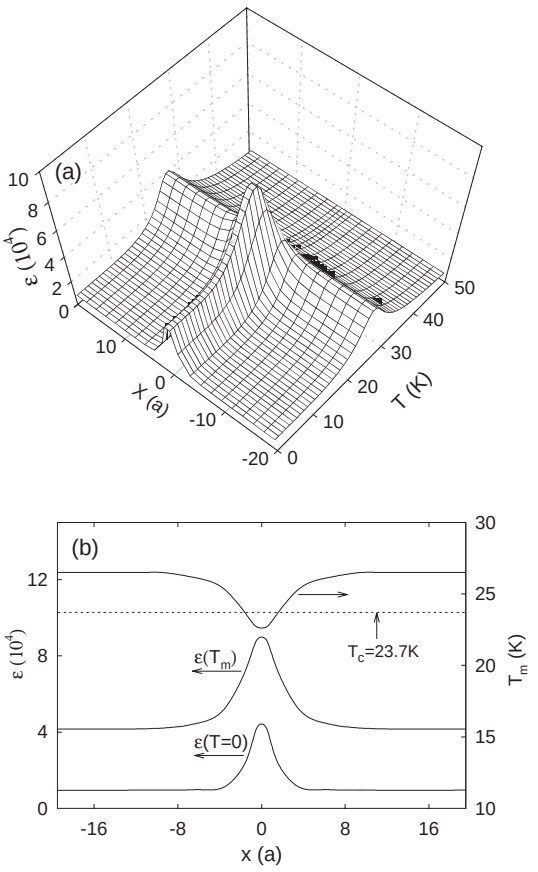

Fig. 6. (a) Temperature dependence of the zero-field dielectric constant at different positions x; (b) x dependencies of $T_{\rm m}$, $\epsilon^{'}(T_{\rm m})$ and $\epsilon'(T=0)$ (see text).

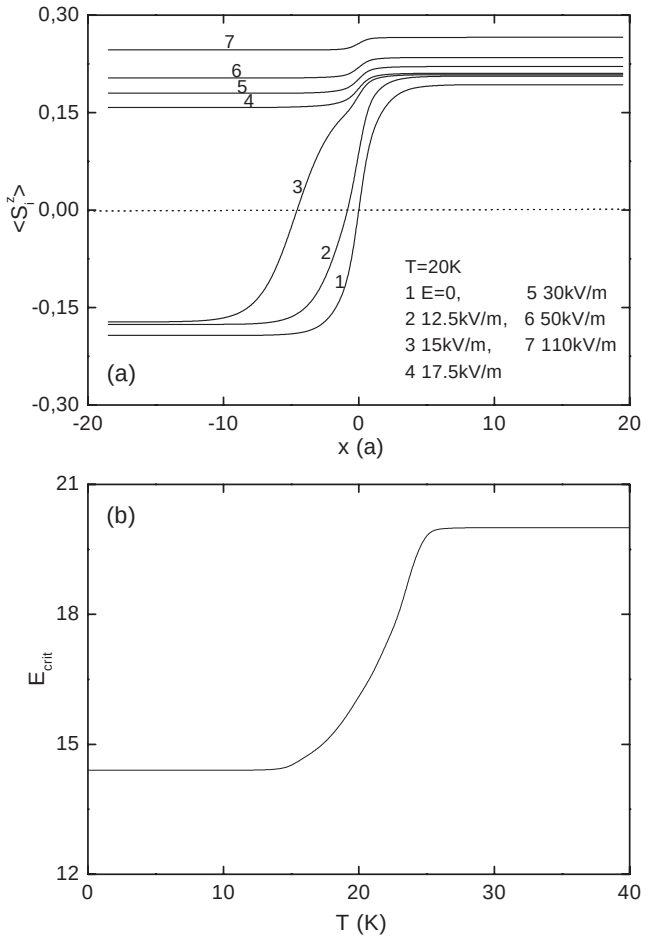

Fig. 7. (a) x dependence of $\langle S_i^z \rangle$ at 20 K under different fields E; (b) temperature dependence of $E_{\rm crit}$.

the sense discussed previously. Clearly, the wall response maximizes for $E \approx E_{\rm frozen}$, where the ac field easily overcomes the depinning threshold. On the other hand, at $E > E_{\rm frozen}$ the walls become depinned by the static field and a single domain state with weak dielectric response gradually emerges. Similar observations are made in our model calculations.

As shown in Figure 5, the bias field induces a secondary low-temperature peak of the susceptibility in STO18. This peak is attributed to the contribution of domain walls as will be clarified in the following. Figure 7a shows the x dependence of $\langle S_i^z \rangle$ on the line (x, 0, 0) at 20 K under different external fields E. They destroy the initial odd symmetry, $\langle S_i^z \rangle_{(-x)} = -\langle S_i^z \rangle_{(+x)}$, which characterizes the case $E = 0$ (curve 1).

When increasing E, the domain wall moves towards $x < 0$ and broadens from $\delta W(E = 0) \approx 2$a to $\delta W(E = 15{\rm kV/m}) \approx 8$a. A rapid reversal of the polarization happens in region $(-)$ as $E \to E_{\rm crit} \approx 16$ kV/m. Thereafter the crystal becomes a single-domain, where small fluctuations of $\langle S_i^z \rangle$ with alternate sign still exist due to the frozen field.

Figure 7b shows the temperature dependence of $E_{\rm crit}$ for STO18. For $T > T_{\rm c} = 24.2$ K, the polarization in the nanodomains is solely due to the frozen field, hence $E_{\rm crit} = E_{\rm frozen} = 20$ kV/m. Below $T_{\rm c}$, it obviously decreases with decreasing temperature until stabilizing at $E_{\rm crit} = 14.5$ kV/m for $T < 14$ K. This tendency is attributed to a capture effect among domains, *i.e.*, a stable domain tends to consume adjacent unstable domains. This domain interaction has an intimate relationship with the polarization near the domain wall. The higher the polarization, the stronger are the interaction and the capture effect. The increase of the capture effect means that $E_{\rm crit}$ will decrease with decreasing T. Below 14 K, the ferroelectric polarization saturates. Hence, the capture effect and $E_{\rm crit}$ become independent of T.

In Figure 8 we consider the domain wall motion induced by temperature under the action of a bias field, $E = 13.7$ kV/m. $\langle S_i^z \rangle$ in the central shell $(20)^-$ is positive near $T_{m1} = 24.2$ K, and abruptly decreases to a negative value below $T = 17$ K. A similar tendency is found in shell $(19)^-$. These processes are obviously due to thermally induced domain wall motion, which controls the appearance of additional domain wall permittivity peaks as seen in Figure 9.

Figure 9a shows the temperature dependence of ϵ' on the line (x, 0, 0) for $E = 13.7$ kV/m. At high temperatures, $T > 30$ K, ϵ' is independent of x. This changes

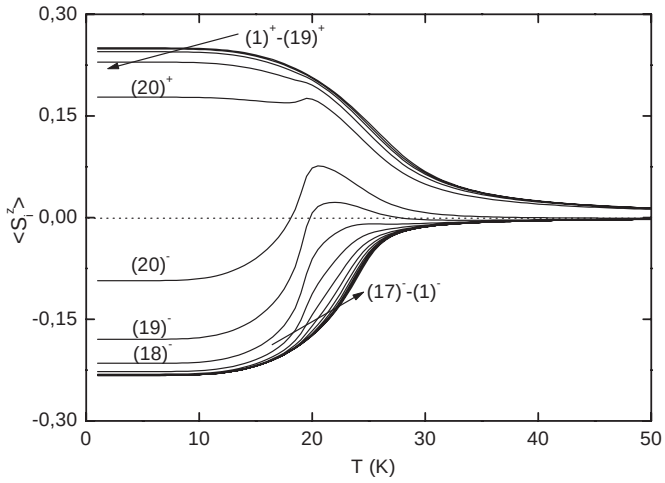

Fig. 8. Temperature dependence of $\langle S_i^z \rangle$ in different shells, $(n^{\pm})$, $1 \leq n \leq 20$, under $E = 13.7$ kV/m.

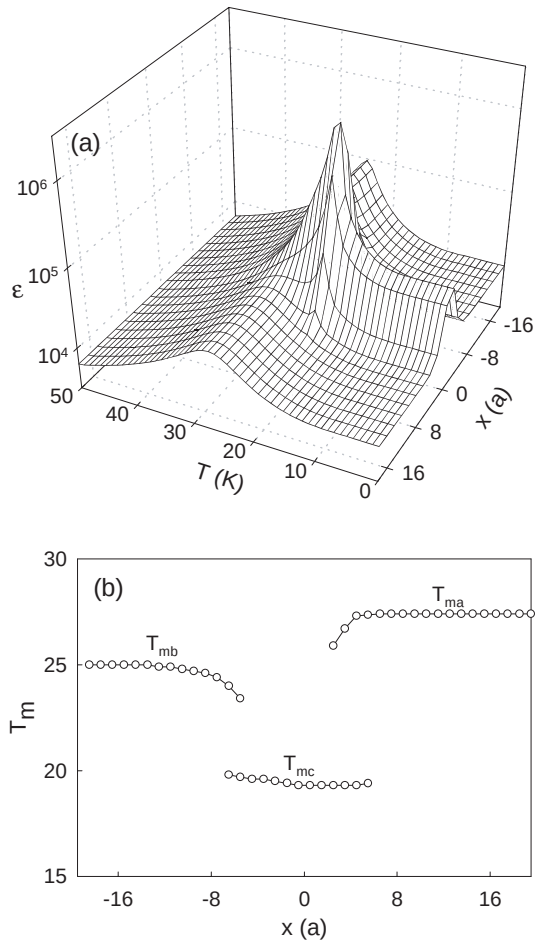

Fig. 9. (a) Temperature dependence of ϵ' at different x for $E = 13.7$ kV/m; (b) x dependencies of T_{ma}, T_{mb} and T_{mc} (see text).

significantly when approaching $T_{m1} \approx 25$ K. In the bulk of the nanodomains ($7.5a \leqslant |x| \leqslant 19.5$a), only the high-temperature peak at $T_{\rm m1}$ is encountered, whereas for $-6.5a \leqslant x \leqslant -5.5a$ or $2.5a \leqslant x \leqslant 6.5a$, we find a double-peak. Finally, within $-4.5a \leqslant x \leqslant 1.5a$, only the low-temperature dielectric peak is observed. Similarly as shown in Figure 6a for $E = 0$, ϵ' is higher in the domain wall than in the bulk when the temperature is very low. This means, again, that the domain wall is always the most active part in the crystal, even if domain wall freezing has happened. Figure 9b shows the x dependence of T_{ma}, T_{mb} and T_{mc}, the temperatures of the high-temperature peaks in regions (+) and (−), and the low-temperature peak near the domain wall, respectively. Since $T_{ma} > T_{mb}$, the bias electric field obviously stabilizes the regions (+) and destabilizes the regions (−) significantly. On the other hand, $T_{\rm mc}$ lies close to the values found for the domain wall instability discussed above (Fig. 8).

Let us finally discuss a relationship between STO18 and relaxors. It is notable that the frequency responses of ϵ' and ϵ'' in Figure 3 are similar to the experimental results of $0.75\mathrm{Pb}(\mathrm{Mg}_{1/3}\mathrm{Nb}_{2/3})\mathrm{O}_3$-$0.25\mathrm{PbTiO}_3$(PMN-PT 0.25) [27]. This similarity is not accidental. Polar clusters and random fields play a key role in relaxors as well as in quantum ferroelectrics [8]. For PMN-PT 0.2, transmission electron microscopy studies [37] show that the size of the polar nano-domains is about 10–15 nm, hence, close to those introduced into our model calculation on STO18. Thus STO18 and PMN-PT seem to have a similar domain structure and, hence, similar relaxational properties. Very probably the different order parameter dimensions of STO18 (probably $n = 2$ as in SrTiO_3:Ca [5]) and PMN-PT ($n = 8$) do not change this result, since in both cases no ferroelectric long-range order is expected [26] and the *RF*s are essentially needed to "organize" the low-T nanodomain state.

In additional calculations (not shown), we have tried to study the domain wall motion qualitatively with changing size of nano-domains. When the size of the nanodomains increases, their stability increases, and the dielectric constant in the domain wall decreases. Thus the effect of the domain walls on the dielectric relaxation will decrease. Obviously, it can be ignored when the domain size tends to infinity. For PMN-PT, experiments [37] show that an increasing content of PT increases the size of nanodomains, and diminishes the degree of relaxor characteristics. Thus our calculation seems to explain the relation between the size and the relaxor characteristics qualitatively also for PMN-PT.

5 Conclusion

Dielectric measurements on STO18 have shown that a *dc* field induces a new polydispersive low-temperature dielectric peak in addition to that at the Curie point. It is shown to be due to domain wall dynamics as derived within the framework of a quantum order-disorder mean-field model including quenched *RF*s. This seems to be adequate to describe the smeared phase transition in isotope-exchanged SrTiO_3. Within a *frozen field* approach we are able to explain the dielectric response and the domain wall motion

induced by a bias field. The model shows that ϵ' is larger in the wall than in the bulk of the domains below the Curie point. In particular, the active domain walls induce a low-temperature dielectric peak below the Curie point as observed experimentally.

Thanks are due to the Alexander von Humboldt-Stiftung for a research grant to Lei Zhang and to the Deutsche Forschungsgemeinschaft (SPP "Strukturgradienten in Kristallen") for financial support.

References

1. K.A. Müller, H. Burkard, Phys. Rev. B **19**, 3593 (1979)
2. K.A. Müller, W. Berlinger, E. Tossatti, Z. Phys. B **84**, 277 (1991)
3. N. Sai, D. Vanderbilt, Phys. Rev. B **62**, 13942 (2000)
4. W.J. Burke, R.J. Pressley, Solid State Commun. **9**, 191 (1971)
5. J.G. Bednorz, K.A. Müller, Phys. Rev. Lett. **52**, 2289 (1984)
6. W. Kleemann, J. Dec, B. Westwański, Phys. Rev. B **58**, 8985 (1998)
7. C. Ang, Z. Yu, P.M. Vilarinho, J.L. Baptista, Phys. Rev. B **57**, 7403 (1998)
8. W. Kleemann, Int. J. Mod. Phys. B **7**, 2469 (1993)
9. M. Itoh, R.P. Wang, Y. Inaguma, T. Yamaguchi, Y.-J. Shan, T. Nakamura, Phys. Rev. Lett. **82**, 3540 (1999)
10. M. Itoh, R.P. Wang, Appl. Phys. Lett. **76**, 221 (2000)
11. R.P. Wang, M. Itoh, Phys. Rev. B **62**, 731 (2000); *ibidem* **64**, 174104 (2001)
12. D.A. Huse, D.S. Fisher, Phys. Rev. B **35**, 6841 (1987)
13. A. Bussmann-Holder, H. Büttner, A.R. Bishop, J. Phys. Cond. Matt. **12**, L115 (2000)
14. O.E. Kvyatkovskii, Solid State Commun. **117**, 455 (2001)
15. K. Abe, K. Yamashita, Y. Tomita, T. Shigenari, R.P. Wang, M. Itoh, *Proc. IMF-10. Madrid, Spain; Ferroelectrics* (to appear)
16. W. Kleemann, A. Albertini, M. Kuss, R. Lindner, Ferroelectrics **203**, 57 (1997)
17. Y.G. Wang, W. Kleemann, W.L. Zhong, L. Zhang, Phys. Rev. B **57**, 13343 (1998)
18. L. Zhang, W.L. Zhong, W. Kleemann, Europhys. Lett. **53**, 401 (2001)
19. R. Blinc, B. Žeks, *Soft modes in ferroelectrics and antiferroelectrics* (North-Holland, Amsterdam, 1974)
20. J. Hemberger, P. Lunkenheimer, R. Viana, R. Böhmer, A. Loidl, Phys. Rev. B **52**, 13159 (1995)
21. W. Kleemann, J. Dec, Y.G. Wang, P. Lehnen, S.A. Prosandeev, J. Phys. Chem. Solids **61**, 167 (2000)
22. J. Dec, W. Kleemann, B. Westwański, J. Phys. Cond. Matt. **11**, L379 (1999)
23. R. P. Wang, M. Itoh (unpublished)
24. R. Viana, P. Lunkenheimer, J. Hemberger, R. Böhmer, A. Loidl, Phys. Rev. B **50**, 601 (1994)
25. H.C. Li, W.D. Si, A.D. West, X.X. Xi, Appl. Phys. Lett **73**, 190 (1998); C. Ang, L.E. Cross, Z. Yu, R.Y. Guo, A.S. Bhalla, *ibidem* **78**, 2754 (2001)
26. Y. Imry, S.K. Ma, Phys. Rev. Lett. **35**, 1399 (1975)
27. A.A. Bokov, Z.G. Ye, Appl. Phys. Lett. **77**, 1888 (2000)
28. J. Dec, unpublished
29. J.H. Barrett, Phys. Rev. **86**, 118 (1952)
30. S.A. Prosandeev, W. Kleemann, B. Westwański, J. Dec, Phys. Rev. B **60**, 14489 (1999)
31. W. Kleemann, A. Albertini, R.V. Chamberlin, J.G. Bednorz, Europhys. Lett. **37**, 145 (1997)
32. E. Courtens, private communication
33. J. Villain, Phys. Rev. Lett. **52**, 1543 (1984)
34. D.P. Belanger, A.P. Young, J. Magn. Magn. Mater. **100**, 272 (1991)
35. E. Sawaguchi, A. Kikuchi, K. Kodera, J. Phys. Soc. Jpn **17**, 1666 (1962)
36. D. Andelman, J.F. Joanny, Phys. Rev. B **32**, 4818 (1985)
37. D. Viehland, M.C. Kim, Z. Xu, J.F. Li, Appl. Phys. Lett. **67**, 2471 (1995)